Carcinogenesis, 2022, **43**, 851–864
https://doi.org/10.1093/carcin/bgac070
Advance access publication 17 August 2022
Original Article

OXFORD

Original Article

Fenretinide combines perturbation of signaling kinases, cell–extracellular matrix interactions and matrix metalloproteinase activation to inhibit invasion in oral squamous cell carcinoma cells

Daren Wang[1], Ping Pei[1], Fortune F. Shea[1], Caroline Bissonnette[1], Kari Nieto[2], Corrine Din[2], Yayuan Liu[2], Steven P. Schwendeman[2], Yan X. Lin[3], Richard Spinney[3] and Susan R. Mallery[1,4,*]

[1]Division of Oral Maxillofacial Pathology & Radiology, College of Dentistry, The Ohio State University, Postle Hall, 305 West 12th Ave, Columbus, OH 43210, USA,
[2]Department of Pharmaceutical Sciences and the Biointerfaces Institute, University of Michigan, North Campus Research Complex, 2800 Plymouth Rd., Ann Arbor, MI 48109, USA,
[3]Department of Chemistry and Biochemistry, The Ohio State University, Columbus, OH 43210, USA and
[4]The Ohio State University Comprehensive Cancer, Columbus, OH 43210, USA

*To whom correspondence should be addressed. Tel: +1 614 292 5892; Email: mallery.1@osu.edu

Abstract

Basement membrane invasion defines malignant transformation of surface premalignancy. Treatment of oral squamous cell carcinoma (OSCC) cells with the synthetic vitamin A derivative, fenretinide (4HPR), induces numerous cancer-preventive effects including suppression of basement membrane invasion, elimination of anchorage-independent growth, disruption of actin cytoskeletal components and inhibition of the invasion-enabling focal adhesive kinase. The purpose of this study was to elucidate 4HPR's effects on additional invasion-relevant mechanisms including matrix metalloproteinase (MMP) activation and function, cell–extracellular matrix (ECM) attachments and interaction with a kinase that is essential for the epithelial–myoepithelial transformation i.e. c-Jun NH2-terminal kinase (JNK). Our data revealed that 4HPR binds with high affinity to the ATP-binding site of all three JNK isoforms with concurrent suppression of kinase function. Additional studies showed 4HPR treatment inhibited both OSCC cell–ECM adhesion and MMP activation and function. JNK downregulation and induced expression studies confirmed that the JNK3 isoform conveyed that largest impact on OSCC migration and invasion. Biodegradable polymeric implants formulated to preserve 4HPR's function and bioavailability were employed to assess 4HPR's chemopreventive impact on an OSCC tumor induction model. These studies revealed 4HPR local delivery significantly inhibited OSCC tumor size, mitotic indices and expression of the endothelial marker, erythroblast transformation-specific-related gene with concurrent increases in tumor apoptosis (cleaved caspase-3). Collectively, these data show that 4HPR suppresses invasion at multiple sites including 'outside-in' signaling, cell–ECM interactions and suppression of MMPs. These functions are also essential for physiologic function. Regulation is therefore essential and reinforces the pharmacologic advantage of local delivery chemopreventive formulations. .

Received: March 14, 2022; Revised: July 1 2022; Accepted: August 16, 2022

Graphical Abstract

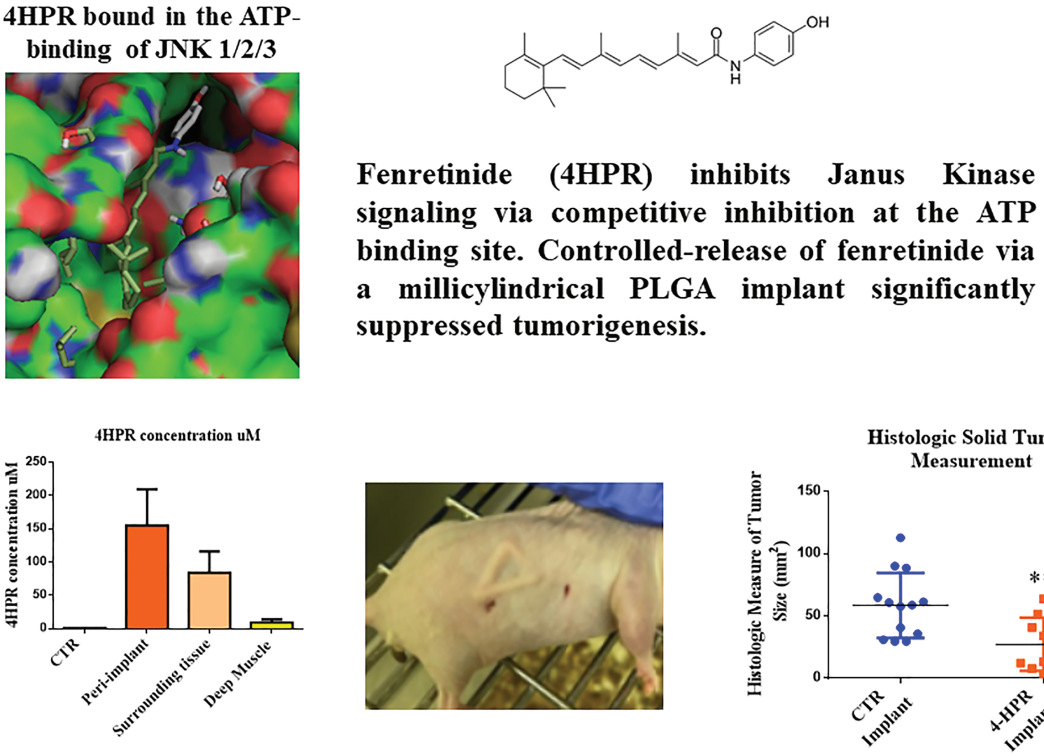

Abbreviations: ECM, extracellular matrix; EGF, epidermal growth factor; EMT, epithelial–myoepithelial transformation; FAK, focal adhesion kinase; MMP, matrix metalloproteinase; OIN, oral intraepithelial neoplasia; OSCC, oral squamous cell carcinoma

Introduction

Invasion of the basement membrane is the defining step whereby preneoplastic epithelial disease progresses to overt carcinoma (1). For many cancers including oral squamous cell carcinoma (OSCC), invasion represents the final step in malignant transformation and conveys the capacity to kill the host (2). In the oral cavity, premalignant epithelial disease, known as oral intraepithelial neoplasia (OIN), encompasses a range of cytologic abnormalities and molecular perturbations contained within the surface epithelium (3). Keratinocyte growth abnormalities including the capacity to modulate the local microenvironment e.g. induction of the 'angiogenic switch' or selective degradation of the extracellular matrix (ECM) increase during progression of OIN to OSCC (4). Although recognized risk factors for OIN malignant transformation are recognized, i.e. higher histologic grade, loss of heterozygosity at putative OIN-relevant tumor-suppressor loci, multiple local recurrences, we still cannot predict which OIN lesions will progress to OSCC (3). As OSCC's devastating effects include loss of tissue vital for esthetics and function and, in many, loss of life, patients with OIN live with the constant underlying concern of malignant transformation (3,5). Another OIN management challenge is the high recurrence rate (recent study >40%) of premalignant oral lesions despite the surgeon obtaining histologically clear margins (5). These recurrence data imply molecular alterations in the repopulating stem cells and establish a need for interventions such as chemoprevention in addition to surgery (6).

Basement membrane invasion is not a trivial undertaking. This complex process entails organized activation of multiple cellular activities including activation of cell–ECM–intracellular signaling, directed activation of matrix metalloproteinases (MMPs), transition to a mobile phenotype and coordination of cytoskeletal components (1). Our laboratory has shown previously that the vitamin A derivative, fenretinide (4HPR), suppresses invasion of a synthetic basement membrane by highly aggressive OSCC cell lines and eliminates anchorage-independent growth (6,7). Additional studies from our laboratory demonstrated 4HPR's abilities to bind with very high affinity to the invasion-enabling focal adhesion kinase (FAK) and disrupt actin cytoskeletal filaments, which provided the mechanistic insights to support 4HPR's inhibition of invasion/tumorigenesis (6). Due to its prognosis-altering effects, suppression of basement membrane invasion is a key secondary OSCC chemoprevention objective (8). The purpose of this study, therefore, is to elucidate 4HPR's effects on additional invasion-relevant parameters including MMP activation and function, cell–ECM attachment and interactions with a signaling kinase i.e. c-Jun NH2-terminal kinase (JNK) that is integral for directed cell migration and the epithelial–mesenchymal transition (EMT) (9,10).

OIN malignant transformation is enabled by gratuitous activation of pro-proliferative, promigratory signaling cascades that enable dysregulated proliferation and transition to a mobile phenotype (10). While JNK is the signaling kinase that activates the *c-jun* proto-oncogene, its role in tumorigenesis is complex and dependent on context, isoform and cell type (10,11). JNK downstream targets include a variety of transcription factors e.g. STAT3, NFAT and ATF-2 that regulate numerous cell functions such as proliferation, differentiation, survival and apoptosis (10–12). Furthermore, JNK's functionally diverse and numerous substrates (>100) enable JNK

to elicit appreciable downstream effects (10–12) in varying scenarios. JNK enzyme function has been determined to be elevated in head and neck squamous cell carcinoma tissue relative to healthy oral mucosa; findings that support translational relevance for further JNK investigation (13). Consistent with the pervasiveness of JNK's protumorigenic effects (associated with pancreatic, non-small cell lung, breast and skin cancers in addition to OSCC), appreciable financial and time investments to identify JNK inhibitors have occurred (14).

While sustained regression of premalignant disease to a normal clinical and histologic appearance is an optimal chemopreventive outcome, complete OIN reversal is not always feasible (3,5,15). For these recalcitrant OIN lesions, restricting disease to an intraepithelial process is a viable chemoprevention strategy. This study describes mechanisms by which 4HPR disrupts promigratory and ECM modulatory pathways that are integral for the final step in malignant transformation i.e. invasion. Accompanying *in vivo* studies, which employed an OSCC tumor induction model, provided key insights regarding chemopreventive capacity of a controlled-release local delivery 4HPR implant.

Materials and methods

Cell culture, validation, JNK siRNA transfection and LV-JNK3 transduction

The JSCC1 and JSCC2 cell lines were derived from microscopically confirmed, primary resection (no prior chemoprevention or radiation exposure) intraoral OSCC obtained in accordance with Ohio State University IRB approval (6). The highly tumorigenic CAL27 ATTC CRL-2095 human tongue OSCC cell line (2095sc), which has been well characterized by our laboratory, was also used (6,7,16). An immortalized, non-tumorigenic cell line derived from HPV16 E6/E7-transduced normal human oral keratinocytes [ScienCell; HOK#2610 (EPI)] was also employed in some experiments. Cell lines were authenticated via short terminal repeat (STR) profiling analyses at the Genetic Resources Core Facility (Johns Hopkins University, Baltimore, MD). All experiments were conducted on low passage vials derived from the STR validated cell lines. In addition, cell lines were negative for mycoplasma (MycoProbe, R&D Systems, Minneapolis, MN). All OSCC cells were cultured in Advanced DMEM (Life Technology, Carlsbad, CA) supplemented with 1× Glutamax and 5% heat-inactivated fetal bovine serum (Gibco; Life Technologies; 'Complete' medium). Serum was omitted ('BASE' medium) during experiments to assess endogenous or growth factor-related effects. Clinical parameters of the primary OSCC tumors, such as the tumor, node, metastases (TNM) classification, presence of perineural and/or vascular invasion and immunohistochemistry (IHC) characterizations have been previously reported (6). 2095sc, JSCC2 and EPI cells were transfected with siRNA (50 nmol/l, Integrated DNA Technologies, Coralville, IA) for JNK1, JNK2, JNK3 and the combination of JNK1/JNK2/JNK3 in complete medium for 12 h. A subset of JSCC2 and 2095sc cells underwent transduction with a either a JNK3 lentivirus (LV-JNK3) or a scrambled lentiviral control (LV-CTR) (OriGene, Rockville, MD) overnight, followed by puromycin selection (1 µg/ml). Transduction effects on JNK3 expression (2095sc-LV-JNK3, JSCC2-LV-JNK3) were determined by immunoblotting. siRNA-treated cells were used for immunoblotting, JNK signaling and the migration and invasion assays. LV-JNK3 and LV-control cells were employed in the migration, invasion and *in vivo* tumorigenesis studies.

JNK function and protein phospho-kinase expression in OSCC cultured cells

4HPR is a generous gift from Dr. Vernon Steele, of the National cancer Institute. Preliminary studies to determine which JNK isoforms are expressed in the OSCC cell cultures revealed that all lines expressed all three isoforms (Supplementary Figure 1A, available at *Carcinogenesis* Online) 2095sc and JSCC2 cells were treated for 24 h in BASE medium with and without 5 µM 4HPR. JNK's ability to phosphorylate its immediate downstream protein was determined using a JNK assay kit (BioVision, Milpitas, CA) with recombinant c-Jun as substrate in the presence of cold ATP. Immunoblotting employed a polyclonal rabbit anti-phospho-c-Jun antibody specific for catalytically activated c-Jun to assess JNK kinase function. In some experiments, cells were pretreated for 2 h with the potent JNK agonist, anisomycin (1 and 10 µM, Fisher Scientific, Waltham, MA). A Li-Cor Odyssey imager and Image Studio software (Li-Cor Biosciences, Lincoln, NE) were used for image capture and analyses, respectively. Additional experiments assessed isoform-specific siRNA-mediated JNK reduction on expression and JNK activity (Supplementary Figure 1B–D, available at *Carcinogenesis* Online).

Following 4HPR treatment, total cell lysates in Complete medium were collected and analyzed using the Proteome Profiler Human Phospho-Kinase Array Kit (ARY003B, R&D Systems, Minneapolis, MN), with image capture and analyses via the LI-COR Odyssey Sa imager and Image Studio software (Li-Cor Biosciences, Lincoln, NE). Subsequent western immunoblots were conducted to assess the effects of 4HPR treatment on expression of proteins that were uniformly modified in both cell lines [(upregulation of: p53, STAT1), (downregulation of: Yes, STAT5a/b, Src)] with GAPDH as the housekeeping protein.

Molecular modeling of 4HPR interactions with JNK, MMP-2, MMP-9 and MT1-MMP

The protein structures of the JNK isoforms and MMPs were obtained from the Protein databank, PDB code 2GMX (http://www.rcsb.org/pdb/home/home.do) (17). The missing JNK and 1CK7 loops were modeled using SwissModel with JNK1 and 1CK7 as templates (18). The structures were optimized with Yasara using the default minimization algorithm (19). As a protein structure with bound ATP was not available, 2GMX was employed as a template, its ligand removed and ATP docked into the binding site (2GMX-ATP). In addition, the apo form of MMP-2 was included due to the large deviation in the backbone configuration on binding of an inhibitor (4.985 Å RMSD between 1CK7 and 1HOV). The optimized protein structure for JNK and ligands was docked using AutoDock Vina using an exhaustiveness of 1000 (20). Each calculation was repeated three times to ensure a thorough exploration of the binding site. Calculated binding free energies were used to determine a binding affinity (Ka) and dissociation constant (Kd) to compare to experimental data. $\Delta G = RT \ln(\mathrm{Ka})$ or $kA = e^{-(\Delta G/RT)}$and Kd = 1/Ka. Since MMP and MTP contain a zinc atom, AutoDock4Zn (20) as implemented in AMDock (21)

were used for docking. A minimum of two docking runs were performed with Ca and Zn charges set at +2 and runs from 10 to 50. Binding affinities as Ki were calculated directly by the software.

Immunoprecipitation and western blotting

JSCC1 and 2095sc OSCC cell lysates (selected due to high endogenous JNK protein levels and cell line tested *in vivo*, respectively) were treated with 0.01, 0.2 and 5 µM 4HPR for 1 hr then solubilized in 1% Triton X (Sigma–Aldrich, St. Louis, MO) buffer + proteinase inhibitors (Thermo Scientific, Waltham, MA). The 4HPR interacting cell proteins (or JNK3 recombinant protein internal control (Sigma, St. Louis, MO) were incubated with the ATP-binding agarose beads (Sigma–Aldrich, St. Louis, MO). The reacting complex (JNK's ATP-binding site with ATP beads) was washed, eluted at room temperature using sodium dodecyl sulfate–polyacrylamide gel electrophoresis loading buffer, followed by a standard immunoblotting protocol. Image analysis was employed using the LI-COR Odyssey Sa and Image Studio software (LI-COR Biosciences, Lincoln, NE) to detect intensities of the fluorescent antibody–immune complex. Crosslinking agents were not used in any of the experiments. Additional experiments entailed assessment of the effects of 4HPR on activation of signaling kinases downstream of JNK.

Evaluation of MT1-MMP, MMP-2 and MMP-9 function

All experiments employed 5 µM 4HPR. The effects of 4HPR on MT1-MMP functional activity were assessed using the MMP activity fluorometric assay kit, with human recombinant MT1-MMP as the functional enzyme (Abcam, Cambridge, MA). 4HPR's effects on gelatinase function (MMP-2 and MMP-9) were assessed using the EnzChek (Molecular Probes-ThermoFisher, Waltham, MA) assay with collagen type IV as the substrate. Data were reported as percentage of remaining enzyme activity (relative to cell line matched control-MMP-2/MMP-9) and relative fluorescent units (MT1-MMP).

Induction of apoptosis

Determination of 4HPR's effect on apoptosis was determined in treated (5 µM 4HPR, 24 h, BASE medium and control 0.1% dimethyl sulfoxide, BASE medium for 24 h) using an assay to determine function of the execution phase enzyme, caspase-3 (Cell Signaling Technologies, Danvers, MA) in accordance with manufacturer's instructions. The assay employed a standard amount of protein per experimental group.

Directed cell migration and invasion

These experiments, which employed a wound healing and invasion of collagen type IV, were conducted as described previously (7). Briefly, the directed migration studies entailed creation of an established size 'wound' in confluent monolayer cultures. Images were obtained using an Apotome Fluorescent microscope (Carl Zeiss) and AxioVision software (Carl Zeiss). Quantitative image analysis of wound closure was determined via ImagePro software (Media Cybernertics). Twenty-four hour sera-starved cells were seeded onto type IV collagen-coated microporous polyester membrane (InnoCyte cell invasion kit, Calbiochem, San Diego, CA) and conditioned medium from the OSCC JSCC-3 cell line (previously determined to be highly chemoattractant to OSCC cells) was placed in the lower well. After 16 h of invasion, cells were formalin fixed, stained with crystal violet and cells in upper chamber removed. ImagePro software was used to quantify the invaded cells.

Assessment of cell adhesion

The Vybrant Cell Adhesion Assay kit (Molecular Probes, Eugene OR) was used to determine 4HPR's effect on ECM adherence. Briefly, cells were treated with 4HPR (5 µM, 24h), loaded with calcein AM (5 µM), placed on precoated 96-well plates (100 µl of 5×10^5 cells), incubated for 2 h, washed and adherent cells measured (485/520 excitation/emission). Results were determined relative to the cell line specific, calcein loaded internal standard curve.

OSCC xenograft chemoprevention studies

For success of a tumor induction model, it was essential to first confirm that the implanted cell line reproducibly formed 2095sc LV-JNK3 cells suspended in 100 µl of Matrigel in the flanks of male nude mice (n = 10), were conducted. By 15 days following cell implantation, all animals had formed tumors, which were histologically confirmed as OSCC at harvest.

For the tumor induction studies, 24 h prior to implantation of SCC2095sc LV-JNK3 cells, 4HPR-releasing polylactide-co-glycolide (PLGA) 50/50 (Resomer RG503H) or drug-free PLGA implants were placed subcutaneously to form a triangle in the murine flank. To ensure 4HPR bioavailability and enhance stability, the PVP–4HPR–TEAC (triethyl-o-acetyl-citrate) implants were formulated to release an amorphous solid dispersion of 4HPR (22). The next day, 1×10^6 SCC2095sc LV-JNK3 in 100 µl of Matrigel were subcutaneously injected into the center of the triangle formed by the PLGA implants in the flanks of 6- to 7-week-old male nude mice (n = 13 control implant, n = 12 4HPR implant). Twenty-three days following cell implantation, the animals were killed and tumors completely excised. Histologic sections through the largest diameter of tumor tissue (generally centrally located) were scanned and surface area calculated via use of the Leica DMi8 microscope, Leica Application Suite X (Buffalo Grove, IL). Tumor volumes (height × width × length of formalin fixed tissue), proliferation [average mitotic activity/10 high power fields (HPF)] and image analysis analyzed levels of cleaved caspase-3 (Image-Pro Premier, Media Cybernetics, Rockville, MD). The pathologist conducting mitotic assessment was blinded to the experimental groups and 10 HPF in three different areas of each tumor were counted. Three additional mice were employed to determine 4HPR levels achieved at the treatment site (two mice-3 4HPR PLGA implants) one mouse PLGA drug-free control implants) all placed in identical fashion as described above. Two additional mice had 4HPR implants placed while one mouse received three drug-free 'blank' implants. Following final tumor measurements, all animals were killed (CO_2 inhalation) 23 days following 2095sc LV-JNK3 implantation. Tumor tissue was fixed for 8 h in buffered formalin, followed by transfer to phosphate-buffered saline. For 4HPR tissue analyses, tissue directly covering the implants, peri-implant tissue and underlying deep skeletal muscle were snap frozen and stored protected from light prior to liquid chromatography–mass spectrometry (LC–MS) analyses.

Determination of JNK signaling *in vivo*

Paraffin embedded tumor tissue sections were deparaffinized, rehydrated and endogenous peroxidase activity was blocked by pretreatment with 3% H_2O_2, followed by microwave processing to facilitate antigen retrieval in Tris-based buffer (pH 9.0). Sections were then blocked with 5% normal serum, 1% BSA, 0.05% Tween-20 in phosphate-buffered saline for 1 h and incubated with anti-c-Jun (phospho S63) antibody (1:250, abcam, Boston, MA) at 4°C overnight. Next the sections were incubated with biotinylated secondary antibodies (1:200, Vector Laboratories) and VECTASTAIN Elite ABC Kit (Vector Laboratories, Burlingame, CA). Immunoreactions were visualized using the DAB substrate, followed by hematoxylin counterstaining. The entire IHC stained slide was scanned (Leica DMi8 Microscope) and assigned a coded number to deidentify the tumor group (control versus treated). A blinded investigator then randomly selected four ×200 image scale fields of the tumor (R and L 4 quadrants top and bottom) to conduct image analyses (Image-Pro Premier 9.2 software, Media Cybernetics, Rockville, MD) of c-Jun (phospho S63).

LC–MS analyses

4HPR concentrations of homogenized murine tissues (1 mg/100 µl phosphate-buffered saline) were spiked with isotopically labeled 4HPR-d4, followed by protein precipitation with cold acetonitrile. LC–MS/MS analyses employed a Thermo Vanquish UHPLC with a TSQ Quantiva mass spectrometer equipped with a heated electrospray ionization source in positive ion mode. 4HPR and its internal standard, 4HPR-d4, were measured by selected reaction monitoring at *m/z* of 392.325 > 283.220 and 396.338 > 283.220, respectively. The linear range established was 0.77–255 µM (300–100 000 ng/g). The quantitation transition was used to report the calculated concentration (ng/ml or ng/g). In order to compare murine tissue 4HPR levels (ng 4HPR/gm tissue) to previously published therapeutic values (i.e. 1–10 µM) mass quantities were converted to micromolar concentrations, as previously published (23–25).

Statistical analyses

A Shapiro–Wilks normality test was used to determine whether parametric (used whenever possible) or non-parametric analyses were employed. Cell adhesion data were evaluated using a two-tailed Wilcoxon matched pairs signed rank test. A one-way ANOVA (Tukey's *post hoc* test) was employed to evaluate results from the collagenase type IV (MMP-2 and MMP-9) functional assay while a Kruskal–Wallis test (Dunn's multiple comparison *post hoc* test) was used to analyze the caspase-3 and MT1-MPP functional activity assays in addition to the directed migration and invasion studies. A Mann–Whitney *U* two-tailed test was employed to assess the effects of lentiviral transduction on directed cell migration, tumor size and *in vivo* JNK signaling while unpaired *t*-tests were used to assess effects of 4HPR implants on OSCC tumor parameters.

Results

4HPR binds with very high affinity to the ATP-binding site of JNK2/3 and with high affinity for JNK1

Molecular modeling studies demonstrated that 4HPR binds with very high affinity to the JNK2/3 and high affinity (JNK1) to the ATP-binding site of JNK isoforms. These data imply that 4HPR functions as a very potent competitive inhibitor for ATP binding in JNK2/JNK3 isoforms and an effective inhibitor for JNK1. Results from the subsequent co-immunoprecipitation studies, which revealed that 4HPR pretreatment inhibited binding of both human recombinant JNK3 and JNK1 along with cell lysates to ATP beads, implies a strong physical interaction between 4HPR and the JNK ATP-binding site (Figure 1A and B). See Supplementary Figure 2, available at *Carcinogenesis* Online for 4HPR-JNK1 immunoprecipitation studies.

4HPR inhibits kinase activity of JNK and suppresses epidermal growth factor-mediated JNK signaling

The JNK functional assay showed that introduction of 4HPR inhibited phosphorylation of JNK's immediate downstream protein (c-Jun) in OSCC cells. While introduction of the potent JNK agonist, anisomycin, increased p-c-Jun levels, inclusion of 4HPR reduced this effect (Figure 1C and D). Studies were conducted in triplicate with comparable results for every assay. Subsequent western immunoblotting studies, which employed epidermal growth factor (EGF) to activate the JNK signaling cascade, revealed time and cell line dependent differences in responsiveness (Figure 2A and Supplementary Figure 3, available at *Carcinogenesis* Online). In contrast, total protein levels, with the exception of c-Jun, remained relatively constant. In both the control and 4HPR-treated cells, c-Jun levels increased slightly at the 2 hr time point.

4HPR modulates phosphorylation and subsequently activation status of protein kinases associated with regulation of aberrant cell growth regulation and suppression of the EMT transition

Data from proteome profiler assays implied 4HPR-induced chemopreventive effects via induction of growth regulatory and/or inhibition of EMT-enabling pathways. Subsequent immunoblotting studies, which showed increases in the growth regulatory protein p53, modest increase in levels of pro-apoptotic immune-enhancing protein STAT1 in one cell line, and reduction in the pro-proliferative, pro-EMT, Src, substantiated the profiling observations (Figure 2B).

4HPR increases activity of the execution phase enzyme caspase-3 in a dose-dependent fashion

4HPR significantly increased caspase-3 functional activity in a dose-dependent fashion (Figure 2C). In addition, cell line dependent differences were observed in that the line with the highest overall proliferation index (2095sc) demonstrated a greater 4HPR-mediated increase in caspase-3 function. siRNA studies revealed that knockdown of the JNK3 isoform had a similar pro-apoptotic effect, as assessed by significantly increased caspase-3 activity, as did 4HPR treatment (Figure 2C).

Cell migration capacity correlates with isoform-specific JNK levels while 4HPR treatment significantly inhibits migration and reduces cell adhesion

All three cell lines showed that siRNA reduction in the JNK3 isoform significantly reduced directed migration capacities and concurrent reduction in all three JNK isoforms had negligible impact. Notably, 4HPR treatment elicited the greatest

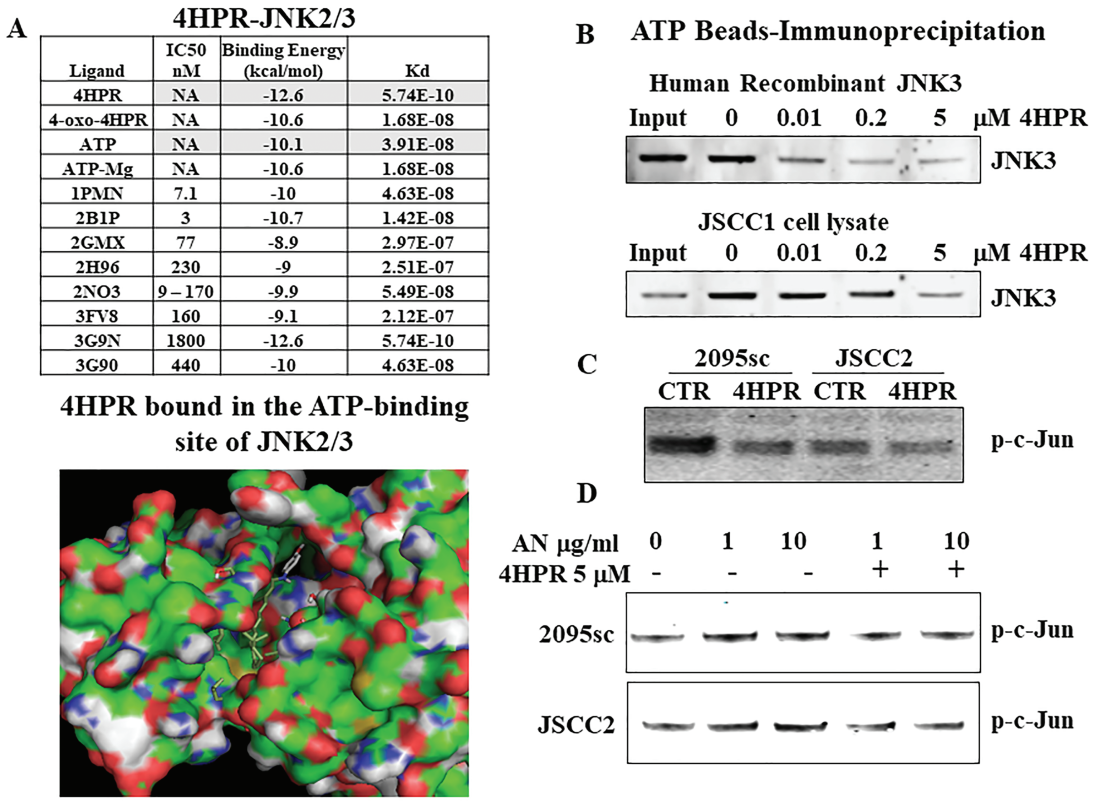

Figure 1. Fenretinide (4HPR) disrupts JNK function via competitive inhibition of ATP binding at the active kinase site. (**A**) Molecular modeling studies, which demonstrated 4HPR interferes with ATP binding in all three JNK isoforms, indicated that 4HPR serves as a very potent ATP competitive inhibitor in JNK 2 and 3 (146× greater affinity than ATP) and an effective JNK1 inhibitor (0.60-fold affinity relative to ATP). The ATP-binding site for the JNK2 and JNK3 isoforms is identical. (**B**) Immunoprecipitation studies that employed ATP agarose beads demonstrated a 4HPR-mediated dose inhibition of JNK ATP bead binding in both human recombinant JNK3 protein and the OSCC cell line, JSCC1 (see Supplementary Figure 1 for JNK1 data). (**C**) 4HPR treatment (5 μM, 24 h) and subsequent binding suppressed JNK function as demonstrated by reduced phosphorylation in JNK's direct downstream kinase, c-Jun. (**D**) OSCC cell lines (2095sc and JSCC2) were pretreated for 1 h with 5 μM 4HPR (or 0.1% dimethyl sulfoxide, control cells) followed by a 30 min challenge with the stress-activated JNK/SAPK kinase activator, anisomycin (AN). Addition of 4HPR suppressed AN-initiated JNK activation.

inhibition of migration (Figure 3A). Conversely, lentivirus-induced overexpression of JNK3 significantly increased cell migratory capacity (Figure 3B). In all three cell lines evaluated (2095sc, JSCC2 and EPI), introduction of 4HPR significantly reduced cellular adherence to the primary oral mucosal basement membrane component, collagen type IV (Figure 3C).

While modulation of JNK levels impacts cell invasion of a synthetic basement membrane, 4HPR elicits the greatest anti-invasive effects

siRNA-mediated decreases in JNK3 along with concurrent reduction in all three JNK isoforms significantly inhibited basement membrane invasion while 4HPR treatment resulted in the highest inhibition of invasion in all cell lines (Figure 4A). In addition, lentiviral-induced JNK3 overexpression significantly augmented invasive capacity (Figure 4B). In all three cell lines evaluated (2095sc, JSCC2 and EPI), introduction of 4HPR significantly reduced cellular adherence to the primary oral mucosal basement membrane component, collagen type IV (Figure 4C).

4HPR perturbs matrix degradation through multiple mechanisms that include inhibition of both MT1-MMP and collagenase IV activity

Molecular modeling studies reveal that 4HPR and its oxidized metabolize 4-oxo-HPR exhibit appreciably lower Ki (higher binding affinity) relative to established MMP and MT1-MMP inhibitors (Figure 5A and B). These modeling data, which show 4HPR very closely approximates the zinc-containing MMP active site, indicate that 4HPR could employ both steric hindrance and hydrophobicity to repel the requisite water molecule necessary for zinc active site function (Figure 5A). Corresponding functional assays demonstrate that 4HPR significantly inhibits both gelatinase (MMP-2 and MMP-9) and MT1-MMP activity in a dose-dependent fashion. Gelatinase was more sensitive enzyme to 4HPR, showing significant inhibition at 2.5 μM 4HPR while 5.0 μM 4HPR was necessary to significantly inhibit MT1-MMP. Also, the premalignant EPI cells showed the overall highest MT1-MMP activity relative to the appreciably lower activity in the OSCC cell lines (Figure 5B) Introduction of 5 μM 4HPR significantly inhibited activity of gelatinases (MMP-2 and MMP-9) associated with collagen type IV degradation. While 4HPR's inhibition was most pervasive at the lower enzyme levels, even at the highest enzyme activity (0.2 U/ml) 4HPR achieved an approximate 50% functional inhibition (Figure 5B).

4HPR controlled-release local delivery implants deliver therapeutically relevant 4HPR levels and significantly inhibit OSCC explant growth, ERG expression and JNK signaling in an OSCC tumor induction model

Placement of controlled-release 4HPR implants resulted in significant inhibition of OSCC tumor size at both the light

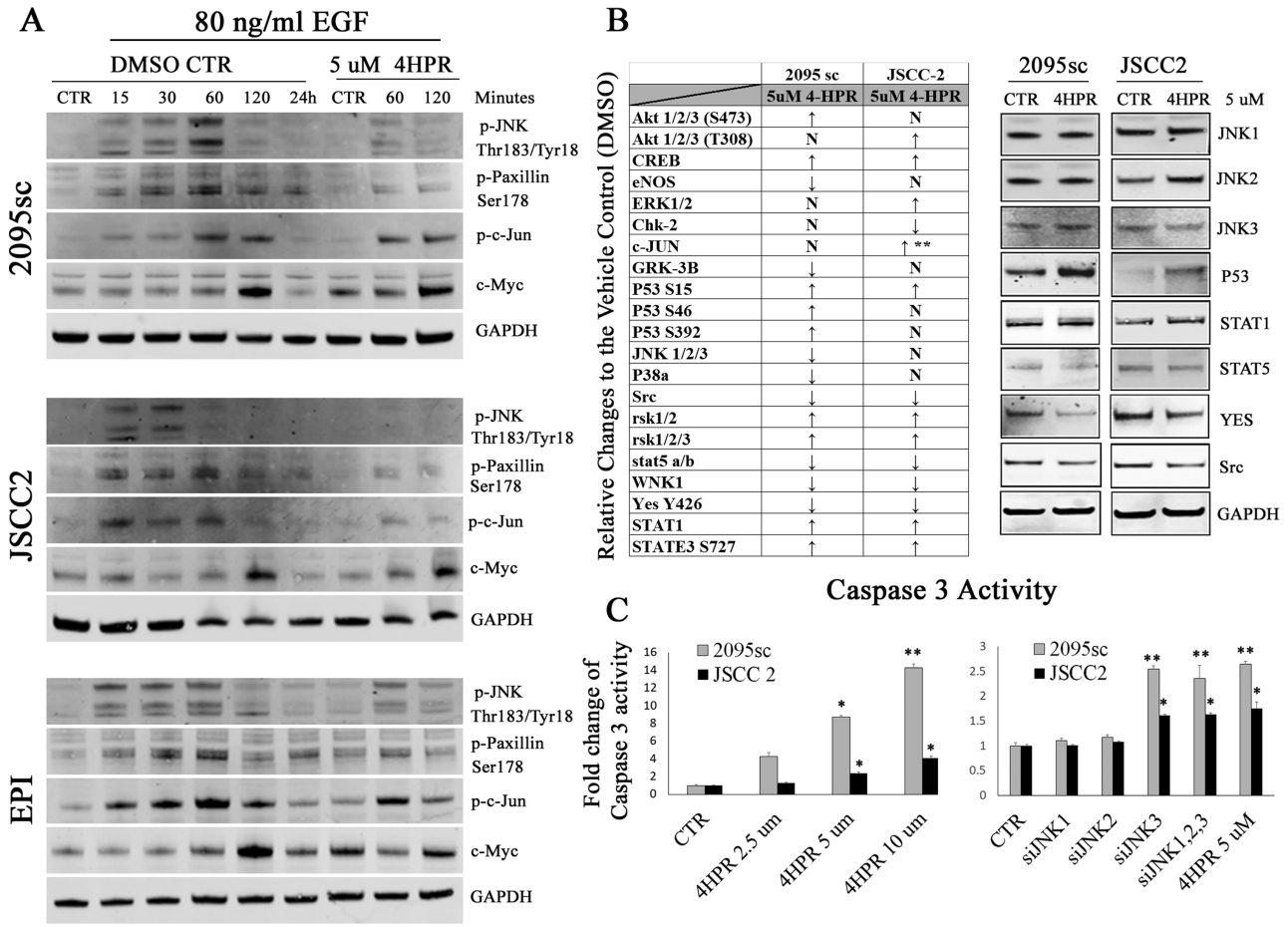

Figure 2. Fenretinide (4HPR) modulates kinase signaling and elicits downstream protein translation and growth modulatory effects. (**A**) Stimulation with EGF (80 μg/ml) initiated the JNK signaling cascade as indicated by increased phosphorylation levels of JNK and its direct downstream targets, Paxillin (pSer178) and c-Jun in a cell line and time-dependent fashion. Introduction of 5 μM 4HPR, however, inhibited this signaling cascade in both OSCC and premalignant oral keratinocytes (EPI). (**B**) Proteome profiler studies revealed that inclusion of 5 μM 4HPR during a 24 h growth period also affected protein activation as indicated by phosphorylation. Corresponding immunoblotting studies demonstrated 4HPR also modulated relevant protein levels. Uniform translational findings in both cell lines showed increases in proteins associated with growth regulation and apoptosis (STAT1, p53), with concurrent downregulation of the pro-proliferative and apoptosis inhibitors YES and Src. (**C**) Consistent with the increases in pro-apoptotic proteins, inclusion of 5 μM 4HPR (24 h treatment) significantly increased function of the execution phase enzyme, caspase-3, in a dose-dependent fashion. Notably, the more aggressive, metastatic cell line (2095sc) demonstrated the greater response to 4HPR-induced apoptosis. In addition, reduction in cellular JNK3 or all JNK isoforms by siRNA increased apoptosis to a level analogous to 4HPR treatment. (n = 5 for every group, Kruskal–Wallis followed by Dunn's multiple comparison *post hoc* test, mean + SEM, *P < 0.05, **P < 0.01).

microscopic and gross levels $P < 0.01$ and $P < 0.05$, respectively (Figure 6A and Supplementary Figure 4, available at *Carcinogenesis* Online). In addition, while all 13 control PLGA implant mice formed tumors, one of the 12 mice with the 4HPR PLGA implants did not have any microscopic tumor at sacrifice. Analyses to determine target tissue levels of 4HPR revealed a gradient with highest 4HPR levels closest to the PLGA implants (peri-implant, ~150 μM), surrounding tissue (site of OSCC explant, ~70 μM) and reduced (~9 μM) in the underlying deep muscle (Figure 6B).

Notably, no adverse effects e.g. ulcration or erosion were observed in the overlying epidermis or adjacent, non-tumor tissues in any of the animals. Furthermore, the 4HPR-releasing PLGA implants inhibited OSCC tumor growth as determined by significant reduction in mitotic figures ($P < 0.010$) while concurrently increasing intratumor levels of the execution phase cleaved caspase-3 ($P < 0.05$) (Figure 6C and D). The presence of the 4HPR implant significantly reduced ERG staining within the OSCC tumors (Figure 6E). While ERG is an excellent endothelial cell marker, ERG also is expressed in granulocytes (26). Accordingly, both endothelial cells and subacutely inflamed granulation tissue that surrounded the tumor demonstrated intense ERG nuclear staining. Notably, scattered OSCC tumor cell nuclei also demonstrated ERG positive staining. Additional studies demonstrated the presence of 4HPR controlled-release implants significantly inhibited JNK signaling as assessed by intranuclear levels of phosphorylated (S63) c-Jun (Supplementary Figure 5, available at *Carcinogenesis* Online, $P < 0.001$, Mann–Whitney U-test). No adverse effects were observed with either the control or 4HPR-releasing implants. The weights of all experimental animals were comparable throughout the study and the skin overlying the OSCC tumor explants remained intact.

Discussion

Invasion is a central process in the development and progression of cancer (1,2). Notably, invasion of an anatomic

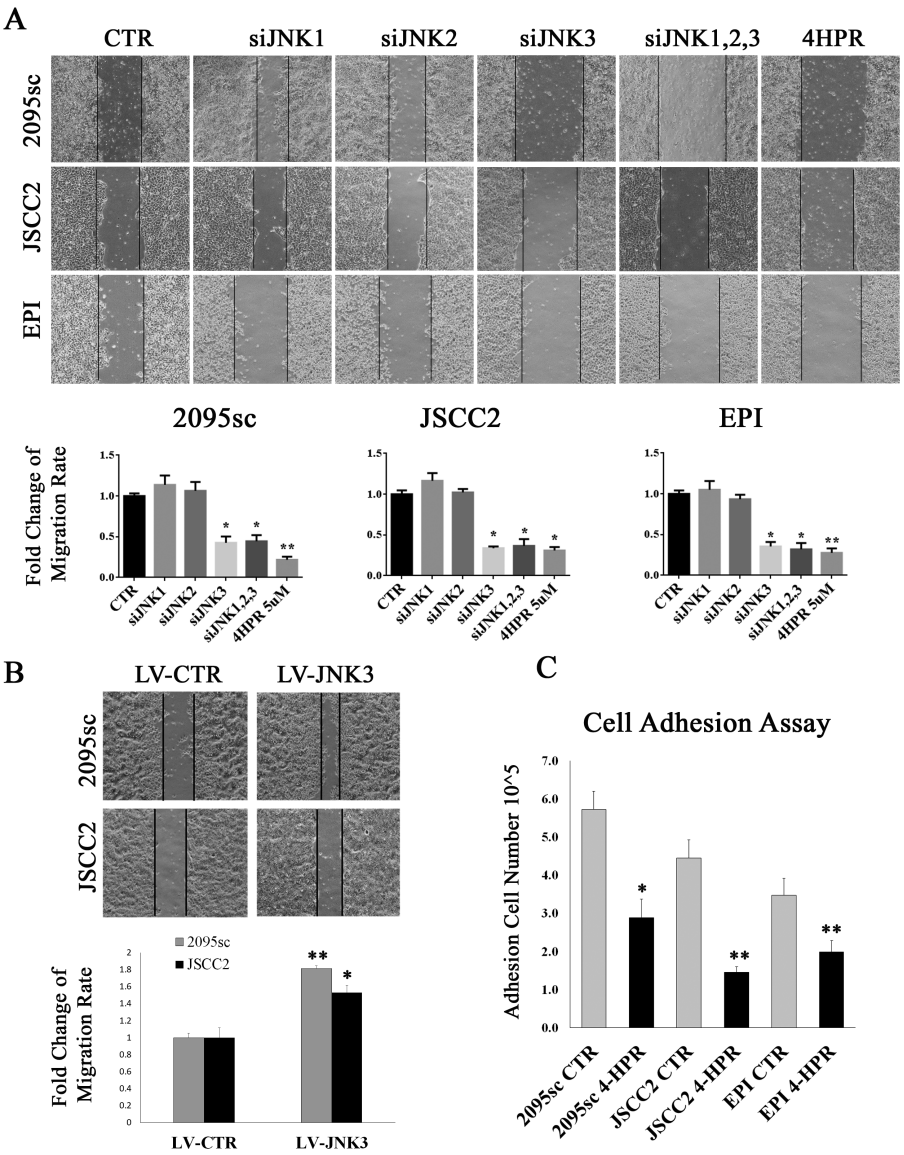

Figure 3. Fenretinide (4HPR) treatment inhibits cell adhesion to a synthetic basement membrane and suppresses transition to a mobile phenotype while modulation of JNK3 can either suppress (siRNA) or augment (lentiviral-induced high expression) migration. (**A**) Protein levels of JNK1, 2 and 3 isoforms were selectively reduced by small interfering RNA treatment of the 2095sc, JSCC2 and EPI cell lines. Corresponding cultures with endogenous levels of JNK were treated with 5 μM 4HPR for 24 h. Results from these wound healing studies revealed a cell line dependence upon a specific JNK isoform i.e. JNK3 for directed migration. Incorporation of 4HPR showed an additional inhibition in two of the three evaluated cell lines (Kruskal–Wallis followed by Dunn's multiple comparison *post hoc* test, $n = 6$ for every group, mean + SEM, $^{*}P < 0.05$, $^{**}P < 0.01$). (**B**) Lentiviral-induced high expression of JNK3 in the OSCC cells significantly increased cell migratory capacity, Mann–Whitney *U*-test, $n = 6$ for both cell lines, mean + SEM, $^{*}P < 0.05$, $^{**}P < 0.01$). (**C**) Following 24 h treatment with 5 μM 4HPR, cells were labeled with calcein AM and plated on collagen type IV. 4HPR treatment significantly disrupted cell adherence (Wilcoxin matched pairs two-tailed sign-rank test, mean + SEM, $n = 6$ 2095sc, JSCC2 and EPI $n = 7$, $^{*}P < 0.05$, $^{**}P < 0.01$).

boundary indicates progression of *in situ* disease to overt carcinoma, while infiltration into underlying lymphatics or blood vessels provides conduits for metastases (1,2). Further, depth of invasion of the primary malignancy is itself a prognostic indicator (27). Results from a multicenter clinical analyses of OSCC primary tumors determined that a depth of invasion >5 mm conveyed a poor prognosis independently of lymph node metastases (27). Clearly, development of an effective strategy to prevent pathologic invasion is critical for both secondary and tertiary chemoprevention. Our findings indicate that 4HPR disrupts invasion at multiple levels including cell–ECM adhesion, directed migration, MMP activation with concurrent inhibition of a signaling kinase (JNK) important for transition to a mobile, ECM-engaging phenotype (28).

Our results revealed a unique role for the JNK3 isoform in OSCC tumorigenesis. While JNK3 studies have been primary focused on brain and neural tissues (29), more recently its unique contributions in carcinogenesis have been appreciated. Studies by Gorogh *et al.* demonstrated that only the JNK3 isoform was capable of conveying chemotherapy resistance and survival in HNSCC cells (30). Additional publications reported the unique contributions of JNK3 in carcinogenesis. Previous analyses of prostate cancer clinical samples confirmed that high intratumor JNK3 levels correlated with a

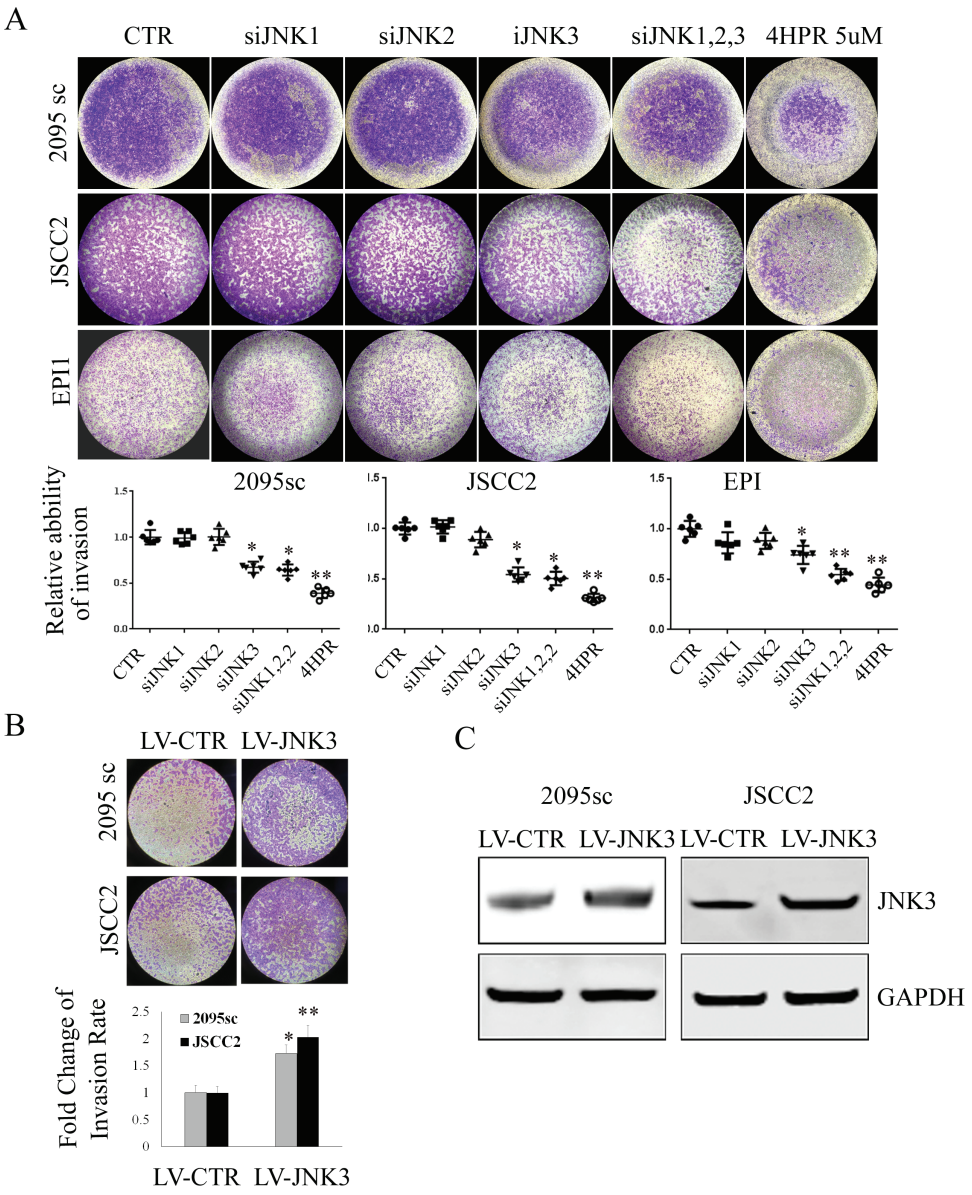

Figure 4. JNK3 is also a critical isoform for invasion of a synthetic basement membrane. (**A**) si-RNA-mediated reduction in JNK isoform proteins also suppressed invasion of a synthetic basement membrane. The highly tumorigenic 2095sc cells demonstrated the greatest invasion capacity and showed significant inhibition of invasion from siRNA-mediated JNK3 reduction. Consistent with its multimodal mechanisms of action (6,7,16,31), 4HPR demonstrated the highest level of invasion suppression across all three cell lines (Kruskal–Wallis one-way ANOVA, followed by the Dunn's multiple comparison test was used for migration and invasion studies, $n = 6$ for every group, mean + SEM, $^{*}P < 0.05$, $^{**}P < 0.01$). (**B**) Consistent with JNK3's recognized role in invasion, lentiviral transduction of JNK3 appreciably enhanced invasion (Mann–Whitney *U*-test, $n = 6$ for every group, mean + SEM, $^{*}P < 0.05$, $^{**}P < 0.01$). (**C**) Immunoblot confirmation of lentiviral-augmented JNK3 expression.

worse prognosis (31). These data, in conjunction with studies from these investigators validated JNK3 as a direct target gene of miR-137-3p in prostate cancer cells, led these investigators to conclude that miR-137-3p exerted a modulatory effect on the JNK3/EZH2 cancer-enabling axis (31). Other investigations by Wu *et al.* conducted in human breast cancer samples and characterized cell lines, determined that JNK3 but not the other JNK isoforms responded to amyloid precursor protein (APP) signaling and that the subsequent JNK3 phosphorylation facilitated the breast cancer cell EMT (32).

Our molecular modeling and immunoprecipitation data show 4HPR binds with high affinity to the functionally essential ATP-binding site of all three JNK isoforms. Similar results i.e. high affinity binding of 4HPR at the ATP-binding site of FAK, c-Src and c-Abl have also been reported by our laboratory (6,7). These data likely reflect preservation of ATP's three-dimensional binding site structure among a diverse group of kinases (33). Collectively, these high affinity ATP-binding site–enzyme inhibitory interactions combined with 4HPR's chemical reactivity conveyed by its electron-rich conjugated dienes and a terminal phenol group support 4HPR's classification as a small molecule protein inhibitor (34).

Our results, which reveal 4HPR suppresses JNK function and downstream signaling, are consistent with 4HPR's occupation and blockage of the ATP-binding site and subsequent prevention of downstream kinase phosphorylation. Interestingly, 4HPR treatment also reduced EGF-mediated JNK phosphorylation; which suggests 4HPR may also suppress an upstream

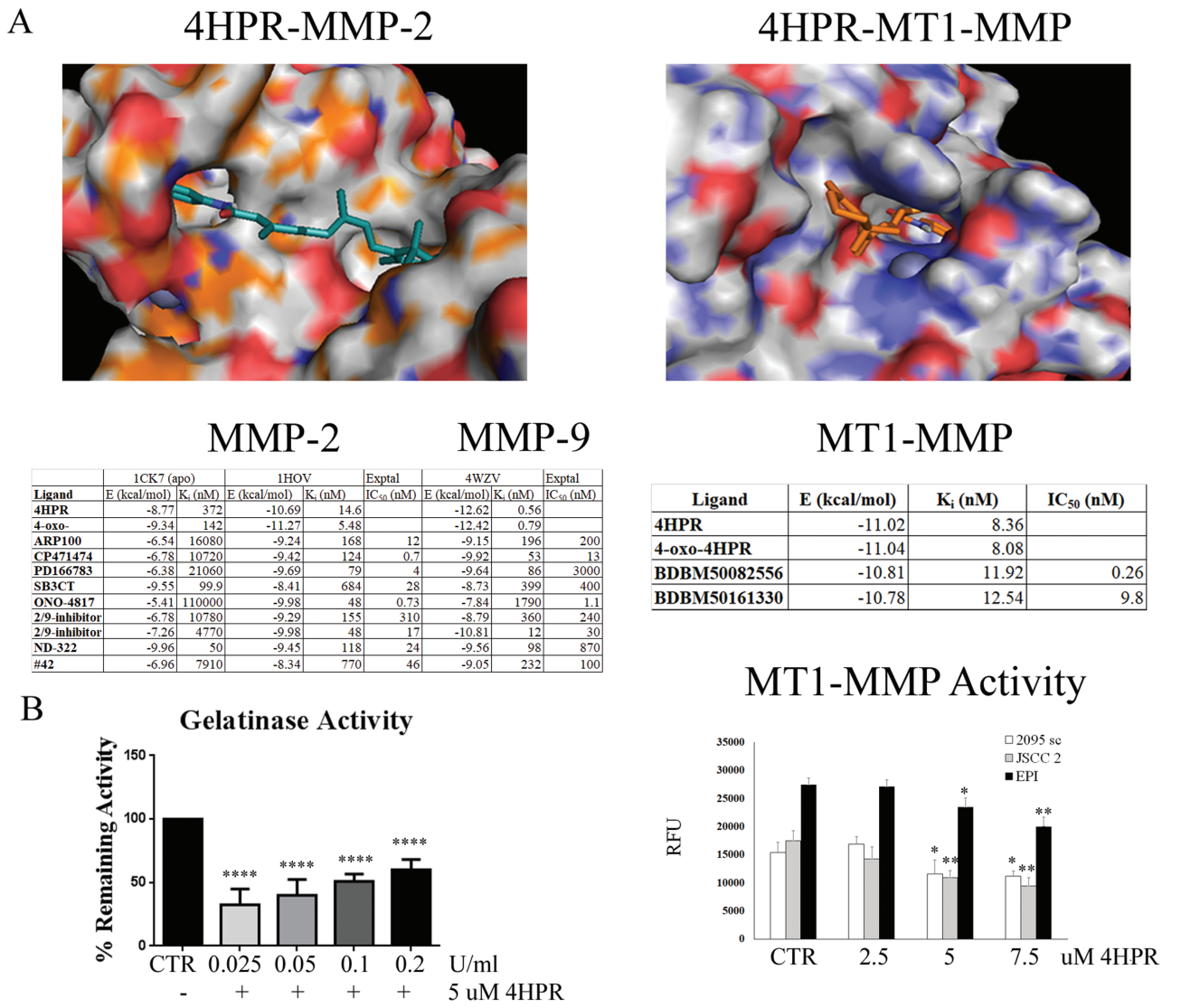

Ligand	1CK7 (apo) E (kcal/mol)	1CK7 (apo) K_i (nM)	1HOV E (kcal/mol)	1HOV K_i (nM)	Exptal IC_{50} (nM)	4WZV E (kcal/mol)	4WZV K_i (nM)	Exptal IC_{50} (nM)
4HPR	-8.77	372	-10.69	14.6		-12.62	0.56	
4-oxo-	-9.34	142	-11.27	5.48		-12.42	0.79	
ARP100	-6.54	16080	-9.24	168	12	-9.15	196	200
CP471474	-6.78	10720	-9.42	124	0.7	-9.92	53	13
PD166783	-6.38	21060	-9.69	79	4	-9.64	86	3000
SB3CT	-9.55	99.9	-8.41	684	28	-8.73	399	400
ONO-4817	-5.41	110000	-9.98	48	0.73	-7.84	1790	1.1
2/9-inhibitor	-6.78	10780	-9.29	155	310	-8.79	360	240
2/9-inhibitor	-7.26	4770	-9.98	48	17	-10.81	12	30
ND-322	-9.96	50	-9.45	118	24	-9.56	98	870
#42	-6.96	7910	-8.34	770	46	-9.05	232	100

Ligand	E (kcal/mol)	K_i (nM)	IC_{50} (nM)
4HPR	-11.02	8.36	
4-oxo-4HPR	-11.04	8.08	
BDBM50082556	-10.81	11.92	0.26
BDBM50161330	-10.78	12.54	9.8

Figure 5. Fenretinide's (4HPR's) inhibition of invasion reflects dual inhibition of MMP activation along with perturbation of MMP function. (**A**) Molecular modeling studies showed both 4HPR and its oxidized metabolite 4-oxo-HPR possess a strong binding affinity for the Zn active site of MT1-MMP, MMP-2 and MMP-9, findings consistent with a strong inhibition of all three enzymes. These analyses imply interactions between retinamide's π-system electrons with the Zn atom. Due to the empirical nature of the modeling software, however, the types of interactions cannot be further delineated. (**B**) Introduction of 5 μM 4HPR also significantly inhibited gelatinases' (MMPs 2 and 9) function in a dose-dependent fashion. Greatest functional inhibition occurred at the highest ratio of 4HPR to gelatinase units of activity (0.025 U/ml), while even at the highest enzyme level (0.2 U/ml), 4HPR inclusion suppressed function to less than 60% of control enzyme function (one-way ANOVA with Tukey's *post hoc* test, mean + SEM, $n = 8$, $^{****}P < 0.0001$). Cell treatment with 4HPR for 24 h revealed a dose dependent decrease in function of the MMP activating enzyme, MT1, with the greatest inhibition occurring at the highest 4HPR (7.5 μM), a level that is achievable by local delivery formulations (29). With regard to MT1-MMP function, the premalignant EPI cell line demonstrated the greatest activity (Kruskal–Wallis one-way ANOVA, followed by the Dunn's multiple comparison test $n = 5$ for every group, mean + SEM, $^{*}P < 0.05$, $^{**}P < 0.01$).

kinase such as PAK and/or MKK3/6. Our data also show EGF stimulation (in the absence of 4HPR) produced two phospho-JNK bands at 46 and 54 kDa; findings that are consistent with alternate splicing as also noted by Okuno *et al.* (35). Our combined proteome profiler, immunoblotting and functional caspase-3 data all demonstrated 4HPR elicited growth regulatory and proapoptotic effects. These findings are consistent with 4HPR's established growth modulatory effects including induction of anoikis, apoptosis and differentiation (7,25,36) and likely reflect 4HPR's perturbation of upstream proliferation-enhancing kinases (6,7,16).

Our data show a positive correlation between JNK levels and cell mobility. These findings compare favorably to the studies of Okada *et al.* (37), who identified a comparable suppression of directed migration/wound healing following JNK inhibition in murine corneal epithelial cells. These investigations also noted the contribution of JNK signaling to both cell adhesion and MMP activation (37). Other studies by Gross *et al.*, which reported increased JNK activity (isoform not specified) in head and neck cancers (HNSCC) relative to clinically healthy tissue, provide clinical relevance (13). This team also demonstrated suppression of HNSCC xenograft growth by the pan-JNK isoform inhibitor SP600125 and showed siRNA JNK1/2 inhibition reduced tumor cell proliferation (13). During health, JNK1 and JNK2 are ubiquitously expressed while JNK3 is predominantly found in brain and to a lesser

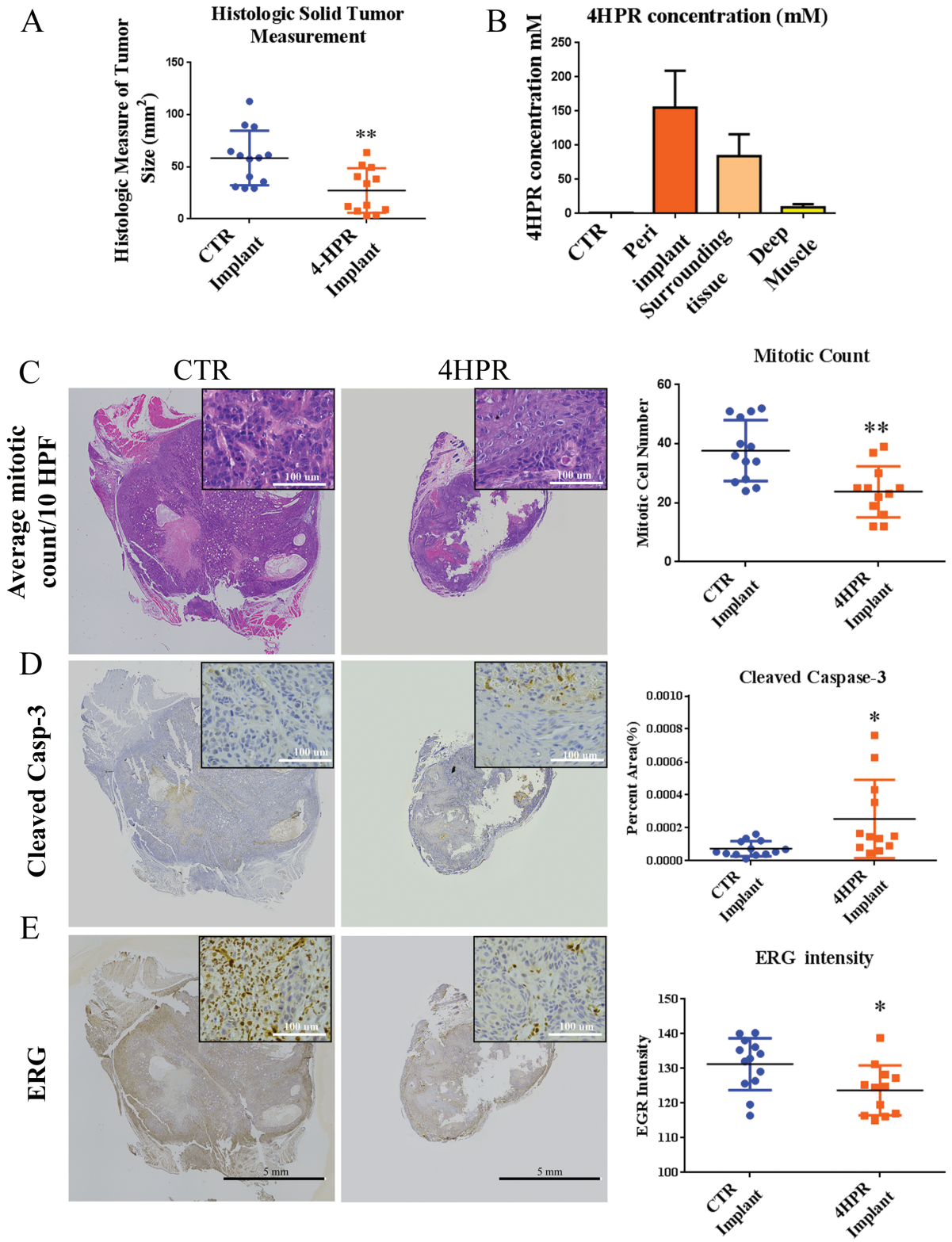

Figure 6. While lentiviral-induced JNK3 overexpression enhances tumorgenicity, controlled fenretinide (4HPR) release from PLGA implants significantly suppresses tumor growth. (**A**) The presence of 4HPR-releasing PLGA implants significantly decreased histologic tumor size ($n = 13$ for CTR, $n = 12$ for 4HPR, $P < 0.01$, unpaired *t*-test). (**B**) 4HPR tissue levels at sacrifice (23 days after implantation) reflected a gradient with highest levels detected at the PLGA cylindrical implant (~150 μM), and intermediate levels found in the surrounding tissue (3–4 mm from implant, ~70 μM, site of OSCC cell implantation). Detectable, albeit lower (~9 μM) 4HPR levels were detected in the deep underlying musculature and no 4HPR was detected in tissue with the control, drug-free, PLGA cylindrical implant. These findings are consistent with 4HPR's protein-binding abilities (44) and imply the potential for a 4HPR drug tissue reservoir during sustained release local delivery. (**C**) The presence of 4HPR PLGA implants significantly ($n = 13$ for CTR, $n = 12$ for 4HPR, $P < 0.01$, unpaired *t*-test) suppressed tumor cell proliferation as determined by mitotic activity. (**D**) Consistent with its well-recognized ability to induce apoptosis (32), the 4HPR implants significantly increased tumor apoptosis ($n = 13$ for CTR, $n = 12$ for 4HPR, $P < 0.05$, unpaired *t*-test) as assessed by expression of the execution phase enzyme caspase-3. (**E**) The 4HPR implant significantly reduced expression of the proto-oncogene ERG in the OSCC tumors ($n = 13$ for CTR, $n = 12$ for 4HPR, $P < 0.05$, unpaired *t*-test). While ERG is recognized as an endothelial marker and associated with angiogenesis, our data also revealed nuclear ERG staining in some of the tumor cells. *$P < 0.05$, **$P < 0.01$.

extent testis and heart (www.proteinatlas.org) (11). Our data, however, demonstrated high basal levels of JNK3 expression in all of our oral keratinocyte cell lines and showed directed migration and invasion were primarily JNK3 dependent. This aberrant oral keratinocyte JNK3 expression may reflect a growth and/or tumorigenic advantage obtained by alternative splicing (38). As *in vitro* data conclusions on JNK3 expression are limited, additional studies to investigate JNK3 levels in OIN lesions and potential contribution to disease progression are ongoing.

4HPR treatment also significantly inhibited cell adhesion to the major constituent of the oral cavity basement membrane i.e. collagen type IV. Cell–ECM interactions, which are contingent upon ECM integrin–cell adhesome–actin–cytoskeletal coordination, represent a key initial stage for cancer cell invasion (39). Previous studies from our laboratory (6) have shown that 4HPR disrupts actin cytoskeletal organization and cortical actin networks while concurrently inhibiting an enzyme crucial for ECM contact and transmission of promigratory–proinvasive integrin signaling i.e. FAK (40). Results from these current studies show 4HPR's inhibition of a second adhesion-promoting enzyme, JNK (37). Interestingly, FAK contributes to growth factor and integrin-initiated activation of the c-jun N-terminal kinase (JNK) (40). This interkinase interaction substantiates FAK–JNK signaling cooperation and supports a multimodal mechanism for 4HPR's anti-invasive effects.

Our data show 4HPR directly inhibits basement membrane invasion at two sequential steps i.e. inhibition of MT-1-mediated MMP activation and direct inhibition of MMP-2 and MMP-9 (collagen type IV degrading gelatinases) function (41). A commonality among the metalloproteinases, inclusive of MT1-MMP, MMP-2 and MMP-9, is the essential active site cofactor, zinc (42). Provided the ability of carotenoids to engage in π-chain electron interactions with metals (43), zinc-chelation is a possible mechanism for 4HPR's MMP inhibition. Another consideration is 4HPR redox activity-initiated interference with the activation-enabling oxidative 'cysteine switch' within the MMP thiol-Zn^{2+} active site (44–46). Our molecular modeling data, however, indicate that while 4HPR closely approximates the catalytic zinc, there are no direct interactions. The most probable mechanism is that 4HPR's binding across the active site Zn blocks access via steric hindrance in conjunction with its hydrophobicity repelling the water molecule necessary for zinc active site interaction (42). A lesser π electron component is likely also involved (43).

In vivo, 4HPR's extreme hydrophobicity raises extensive delivery/drug distribution challenges. Without the benefit of agents to preserve solubility and prevent crystallization, 4HPR rapidly crystallizes and becomes biologically inert (47). The PLGA local delivery formulations used in this study, however, incorporated polyvinylpyrrolidone (PVP) and TEAC to ensure that 4HPR remained in an amorphous solid dispersion (22) and readily bioavailable to the OSCC explants. The pharmacokinetics of the PVP–4HPR–TEAC implants have been well characterized both *in vitro* and *in vivo* (22). Following an initial burst, 4HPR implant release *in vivo* was slow, continuous and resulted in nearly complete drug release (0.25 mg 4HPR loaded per implant) after 30 days (22). Based on these release data and 4HPR's established high protein-binding affinity (48), which would help retain drug at the treatment site, a triangular implant placement design was employed, resulting in final target tissue 4HPR drug levels of ~70 μM at 26 days. Notably, results from our tumor induction studies confirmed the 4HPR implants delivered bioactive and therapeutically relevant 4HPR levels.

Due to 4HPR's extreme hydrophobicity and subsequent crystallization/inactivation if not maintained in a soluble state (such as occurs with bolus 4HPR delivery) (47) this study compared the effects of a PLGA drug-free control implant relative to a 4HPR-releasing implant on OSCC xenograft growth. 4HPR implant placement significantly reduced OSCC tumor size, mitotic activity and JNK signaling with concurrent increased apoptosis (assessed by intratumor cleaved caspase-3). These positive data reflect a variety of 4HPR tumor-suppressive mechanisms that include growth state modulation from a proliferative to differentiated state (increased keratinization and elevated apoptosis), reduced cell motility and invasion and perturbation of endothelial cell signaling and migration resulting in decreased angiogenesis (49). Interestingly, some of the OSCC tumor cells showed ERG nuclear expression. While expression of the proto-oncogene ERG has been documented in human carcinomas including renal cell carcinoma and cervical cancer where it conveys an unfavorable prognosis-ERG has not been reported in OSCC/HNSCC (www.proteinatlas.org). Of note, the proto-oncogene ERG engages in chromosomal translocations that generate fusion gene products; a process that is best characterized in prostate cancer (50). While the significance of our observation remains to be determined, the potential for a novel ERG gene fusion protein associated with OSCC warrants further study.

Although our data support a role for JNK in OSCC tumorigenesis, correlative clinical data are needed to convey translational impact. A recent study by Badarni *et al.* helped to clarify JNK's protumorigenic function in squamous cell carcinoma of the head and neck (HNSCC) (51). These investigators determined that concurrent JNK inhibition in combination with anti-PI3K therapy was necessary to suppress AP-1 upregulation of AXL and resulted in reduced tumor growth in both HNSCC patient-derived xenografts and syngeneic HNSCC murine models (51). As the TAM family member AXL is associated with many aspects of tumorigenesis including proliferation, EMT, metastases and angiogenesis, its inhibition has been proposed as a promising therapeutic approach (52). An additional investigation determined that MAPK/JNK activation is associated with the development of cetuximab resistance following SMAD4 loss in HNSCC patients (53).

Collectively, our data from this study and previous publications show that 4HPR aborts invasion at multiple sites including inhibition of 'outside-in' signaling and cell–ECM interactions, perturbation of actin polymerization, disruption of invasion-enabling signaling cascades and suppression of MMP activation and function (6,7,16). Because these mechanisms are also essential for physiological functions, e.g. wound healing, the capacity to selectively inhibit invasion is key. Our *in vivo* data, which demonstrate local 4HPR delivery via a 4HPR-ASD PLGA implant suppresses OSCC tumorigenesis without adverse local or systemic effects, reinforce the pharmacologic advantage of local delivery chemopreventive formulations.

Supplementary material

Supplementary data are available at *Carcinogenesis* online.

Supplementary Figure 1. (**A**) Immunoblotting studies on log growth cultured OSCC cells revealed every OSCC cell line expressed all three JNK isoforms, albeit at different levels. (**B** and **C**) JNK knockdown studies confirmed the isoform specificity of the siRNA treatment in 2095sc and EPI cells. (**D**) In addition, siRNA treatment downregulated JNK activity as demonstrated by reduced phosphorylation in JNK's direct downstream effector, c-Jun. Individual immunoblot band intensity was quantitatively analyzed using Image-Pro Premier software (Media Cybernetics). Notably, siRNA directed against all three JNK isoforms did not completely eliminate p-c-Jun levels. These cell lysate data could reflect the inability of siRNA to completely eliminate JNK protein and/or the activity of other kinases such as Cdk2 that are also capable of phosphorylating c-Jun p63 and p73 residues.

Supplementary Figure 2. 4HPR exhibits a lower binding affinity at the JNK1 ATP-binding site relative to the common ATP-binding site shared by the JNK2 and JNK3 isoforms. As confirmed by the molecular modeling data this interaction was sufficient to enable 4HPR to serve as a strong JNK1 inhibitor. Similar to the JNK2/3 isoforms, 4HPR inclusion resulted in a dose-dependent reduction in human recombinant JNK1 ATP binding. These data, in conjunction with data shown in Figure 1, support 4HPR's function as a competitive inhibitor of the JNK ATP-binding site.

Supplementary Figure 3. Stimulation with EGF (80 µg/ml) initiated the JNK signaling cascade as indicated by increased phosphorylation levels of JNK and its direct downstream targets, Paxillin (pSer178) and c-Jun in a cell line and time-dependent fashion (see Figure 2). In contrast with the marked changes noted in phosphorylated protein levels, total protein levels, with the exception of c-Jun, remained relatively constant. In both the control and 4HPR-treated cells, c-Jun levels increased slightly at the 2 hr time point. While the significance of this finding is uncertain, it may reflect c-Jun's function as a central signaling hub of the AP-1 complex.

Supplementary Figure 4. (**A**) Polylactide-co-glycolide (PLGA) millicylindrical implants that provide a sustained release of bioavailable and bioactive 4HPR were implanted into the dorsal skin of nude mice. Twenty-four hours later, 1×10^6 SCC2095sc LV-JNK3 cells, suspended in 100 µl of Matrigel, were subcutaneously injected at this site. (**B**) The presence of 4HPR PLGA cylindrical implants significantly decreased gross tumor volume ($n = 13$ for CTR, $n = 12$ for 4HPR, $P < 0.05$, unpaired *t*-test) relative to drug-free PLGA cylindrical implants.

Supplementary Figure 5. 1×10^6 SCC2095sc LV-JNK3 cells, suspended in 100 µl of Matrigel, were subcutaneously injected in the flank of nude mice. PLGA implants (drug-free control and 4HPR controlled release) were placed at the proposed site 24 h prior to the murine tumor cell implantation. The presence of 4HPR-releasing PLGA implants significantly reduced nuclear translocation of p-c-Jun in the OSCC tumors ($n = 13$ for CTR, $n = 12$ for 4HPR, $P < 0.001$, unpaired *t*-test).

Funding

National Institute of Health-National Cancer Institute (R01CA227273 and R01CA211611 to S.R. Mallery).

Acknowledgements

The authors would like to acknowledge the assistance provided by Ms Mary Marin and Ms Merritt Bernath for their histotechnologic expertise in sectioning of the fixed tumor tissues. The costs of publication of this article were defrayed in part by the payment of page charges. This article must therefore be hereby marked advertisement in accordance with 18 U.S.C. Section 1734 solely to indicate this fact.

Conflict of Interest Statement: Drs Mallery and Schwendeman have a US patent under review. 'Chemoprevention Using Controlled-Release Formulations or Anti-Interleukin 6 Agents, Synthetic Vitamin A Analogues or Metabolites and Estradiol Metabolites'. Pub No: US 2019/0091330 A1. Pub Date: 3/28/19.

Authors' contributions

D. Wang: conceptualization, data curation, formal analysis, validation, investigation, visualization, methodology, writing–review and editing. P. Pei and F. Shea: data curation, formal analysis, validation, investigation, visualization and methodology. C. Bissonette: investigation and visualization. K. Nieto, C. Din, Y. Liu, S.P. Schwendeman and Y.X. Lin: investigation, visualization and methodology. R. Spinney: software, investigation, visualization and methodology. S.R. Mallery: conceptualization, resources, project administration, supervision, formal analysis, funding acquisition, validation, visualization, writing–original draft, project administration and writing–review and final editing.

References

1. Liotta, L.A. et al. (2016) Adhere, degrade, and move: the three-step model of invasion. *Cancer Res.*, 76, 3115–3117.
2. Liotta, L.A. et al. (1980) Metastatic potential correlates with enzymatic degradation of basement membrane collagen. *Nature*, 284, 67–68.
3. Woo, S.B. et al. (2019) Oral epithelial dysplasia and premalignancy. *Head Neck Pathol.*, 13, 423–439.
4. Baeriswyl, V. et al. (2009) The angiogenic switch in carcinogenesis. *Semin. Cancer Biol.*, 19, 329–337.
5. Sundberg, J. et al. (2019) Recurrence rates after surgical removal of oral leukoplakia—a prospective longitudinal multicentre study. *PLoS One*, 6, 14–26.
6. Han, B. et al. (2015) Fenretinide perturbs focal adhesion kinase in premalignant and malignant human oral keratinocytes. Fenretinide's chemopreventive mechanisms include ECM interactions. *Cancer Prev. Res.*, 8, 419–430.
7. Mallery, S.R. et al. (2017) Benefits of multifaceted chemopreventives in the suppression of the oral squamous cell carcinoma (OSCC) tumorigenic phenotype. *Cancer Prev. Res.*, 10, 76–88.
8. Kumar, K.V. et al. (2019) Extracellular matrix in invasion and metastasis of oral squamous cell carcinoma. *J. Oral Maxillofac. Pathol.*, 23, 10–16.
9. Cai, J. et al. (2017) Tenascin-C induces migration and invasion through JNK/c-Jun signaling in pancreatic cancer. *Oncotarget*, 8, 74406–74422.
10. Gkouveris, I. et al. (2017) Role of JNK signaling in oral cancer: a mini review. *Tumor Biol.*, 6, 39–45.
11. Tournier, C. et al. (2013) The 2 faces of JNK signaling in cancer. *Genes Cancer*, 4, 397–400.
12. Zeke, A. et al. (2016) JNK signaling: regulation and functions based on complex protein-protein partnerships. *Mol. Microbiol. Rev.*, 80, 793–835.

13. Gross, N.D. et al. (2007) Inhibition of Jun NH2-terminal kinases suppresses the growth of experimental head and neck squamous cell carcinoma. *Clin. Cancer Res.*, 13, 5910–5917.
14. Wu, Q. et al. (2020) Selective inhibitors for JNK signaling: a potential targeted therapy in cancer. *J. Enzyme Inhib. Med. Chem.*, 35, 574–583.
15. Ranganathan, K. et al. (2019) Oral epithelial dysplasia: classifications and clinical relevance in risk assessment of oral potentially malignant disorders. *J. Oral Maxillofac. Pathol.*, 23, 19–27.
16. Mallery, S.R. et al. (2019) The combination of fenretinide, tocilizumab & reparixin provide multifaceted disruption of oral squamous cell carcinoma stem cell properties: implications for tertiary chemoprevention. *Mol. Cancer Ther.*, 18, 2308–2320.
17. Szczepankiewicz, B.G. et al. (2016) Aminopyridine-based c-Jun N-terminal kinase inhibitors with cellular activity and minimal cross-kinase activity. *J. Med. Chem.*, 49, 3563–3580.
18. Waterhouse, A. et al. (2018) SWISS-MODEL: homology modelling of protein structures and complexes. *Nucleic Acids Res.*, 46, 296–303.
19. Krieger, E. et al. (2002) Increasing the precision of comparative models with YASARA NOVA—a self-parameterizing force field. *Proteins*, 47, 393–402.
20. Santos-Martins, D. et al. (2014) AutoDock4Zn: an improved AutoDock force field for small-molecule docking to zinc metalloproteins. *J. Chem. Inf. Model.*, 54, 2371–2379.
21. Valdés-Tresanco, M.S. et al. (2020) AMDock: a versatile graphical tool for assisting molecular docking with Autodock Vina and Autodock4. *Biol. Direct*, 15, 12. doi: 10.1186/s13062-020-00267-2.
22. Nieto, K. et al. (2020) Microencapsulation of amorphous solid dispersions of fenretinide enhances drug solubility and release from PLGA in vitro and in vivo. *Int. J. Pharm.*, 586, 119475.
23. *Bioanalytical Method Validation. Guidance for Industry*. U.S. Department of Health and Human Services, Food and Drug Administration, Center for Drug Evaluation and Research (CDER), Center for Veterinary Medicine (CVM). Biopharmaceutics, 2018. https://www.fda.gov/media/70858/download
24. Cho, H.E. et al. (2017) Analysis of fenretinide and its metabolites in human plasma by liquid chromatography-tandem mass spectrometry and its application to clinical pharmacokinetics. *J. Pharm. Biomed. Anal.*, 132, 117–124.
25. Holpuch, A. et al. (2012) Evaluation of a mucoadhesive fenretinide patch for local intraoral delivery: a strategy to reintroduce fenretinide for oral cancer chemoprevention. *Carcinogenesis*, 33, 1098–1105.
26. Olson, N.J. et al. (2020) Survey of ERG expression in normal bone marrow and myeloid neoplasms. *J. Hematopathol.*, 13, 5–12.
27. Ebrahimi, A. et al. (2014) Primary tumor staging for oral cancer and a proposed modification incorporating depth of invasion: an international multicenter retrospective study. *JAMA Otolaryngol. Head Neck Surg.*, 140, 1138–1148.
28. Huang, C. et al. (2004) MAP kinases and cell migration. *J. Cell Sci.*, 117, 4619–4628.
29. Nakano, R. et al. (2020) Biological properties of JNK3 and its function in neurons, astrocytes, pancreatic β-cells and cardiovascular cells. *Cells*, 9, 1802. doi: 10.3390/cells9081802.
30. Gorogh, T. et al. (2004) Differential regulation of MAPK (JNK 3) gene expression in human head and neck squamous cell carcinomas. *Onkologie*, 4, 353–357.
31. Zang, Y. et al. (2020) miR-137-3p modulates the progression of prostate cancer by regulating the JNK3/EZH2 axis. *Onco Targets Ther.*, 13, 7921–7932.
32. Wu, X. et al. (2020) Amyloid precursor protein promotes the migration and invasion of breast cancer cells by regulating the MAPK signaling pathway. *Int. J. Mol. Med.*, 1, 162–174.
33. Ghosh, A.K. et al. (2019) Covalent inhibition in drug discovery. *ChemMedChem*, 14, 889–906.
34. McFedries, A. et al. (2013) Methods for the elucidation of protein-small molecule interactions. *Chem. Biol.*, 20, 667–673.
35. Okuno, S. et al. (2004) The c-Jun N-terminal protein kinase signaling pathway mediates Bax activation and subsequent neuronal apoptosis through interaction with Bim after transient focal cerebral ischemia. *J. Neurosci.*, 24, 7879–7887.
36. Janardhanan, R. et al. (2008) N-(4-Hydroxyphenyl) retinamide induced differentiation with repression of telomerase and cell cycle to increase interferon gamma sensitivity for apoptosis in human glioblastoma cells. *Cancer Lett.*, 261, 426–436.
37. Saika, O.Y. et al. (2009) JNK MAPK signaling contributes in vivo to injury-induced corneal epithelial migration. *Ophthalmic Res.*, 42, 185–192.
38. Zhang, Y. et al. (2021) Alternative splicing and cancer: a systematic review. *Signal Transduct. Target. Ther.*, 6, 78. doi: 10.1038/s41392-021-00486-7.
39. Gkretsi, V. et al. (2018) Cell adhesion and matrix stiffness: coordinating cancer cell invasion and metastasis. *Front. Oncol.*, 8, 145. doi: 10.3389/fonc.2018.00145. PMCID: PMC5945811.
40. Hauck, C.R. et al. (2002) The focal adhesion kinase—a regulator of cell migration and invasion. *IUBMB Life*, 53, 115–119.
41. Gkouveris, I. et al. (2017) Matrix metalloproteinases in head and neck cancer: current perspectives. *Metalloproteinases Med.*, 4, 47–61.
42. Loffek, S. et al. (2011) Biological role of matrix metalloproteinases: a critical balance. *Eur. Respir. J.*, 38, 191–208.
43. Horiuchi, S. et al. (2015) Multinuclear metal-binding ability of a carotene. *Nat. Commun.*, 6, 6742. doi: 10.1038/ncomms7742.
44. Khrenova, M.G. et al. (2014) Exploration of the zinc finger motif in controlling activity of matrix metalloproteinases. *J. Phys. Chem.*, 118, 13505–13512.
45. Pei, P. et al. (2006) Reduced nonprotein thiols inhibit activation and function of MMP-9: implications for chemoprevention. *Free Radic. Biol. Med.*, 41, 1315–1324.
46. Du, Y. et al. (2014) Fenretinide targets chronic myeloid leukemia stem/progenitor cells by regulation of redox signaling. *Antioxid. Redox Signal.*, 20, 1866–1880.
47. Nieto, K. et al. (2018) In vivo controlled release of fenretinide from long-acting release depots for chemoprevention of oral squamous cell carcinoma recurrence. *Int. J. Pharm.*, 538, 48–56.
48. Berni, R. et al. (1992) In vitro interaction of fenretinide with plasma retinol-binding protein and its functional consequences. *FEBS Lett.*, 308, 43–45.
49. Yücel, E.I. et al. (2020) Fenretinide reduces angiogenesis by downregulating CDH5, FOXM1 and eNOS genes and suppressing microRNA-10b. *Mol. Biol. Rep.*, 47, 1649–1658.
50. Adamo, P. et al. (2016) The oncogene ERG: a key factor in prostate cancer. *Oncogene*, 35, 403–414.
51. Badarni, M. et al. (2019) Repression of AXL expression by AP-1/JNK blockage overcomes resistance to PI3Ka therapy. *JCI Insight*, 5, 125341.
52. Zhu, C. et al. (2019) AXL receptor tyrosine kinase as a promising anti-cancer approach: functions, molecular mechanisms and clinical applications. *Mol. Cancer*, 18, 1–12.
53. Ozawa, H. et al. (2017) SMAD4 loss is associated with cetuximab resistance and induction of MAPK/JNK activation in head and neck cancer cells. *Clin. Cancer Res.*, 17, 5162–5175.